

¹ To the Graduate Council:
² I am submitting herewith a thesis written by Jason Bane entitled “The EMC Effect
³ in A=3 Nuclei.” I have examined the final paper copy of this thesis for form and
⁴ content and recommend that it be accepted in partial fulfillment of the requirements
⁵ for the degree of Doctor of Philosophy, with a major in Nuclear Physics.

⁶
⁷

Nadia Fomin, Major Professor

⁸ We have read this thesis
⁹ and recommend its acceptance:

¹⁰ _____

¹¹ Jamie Coble

¹² _____

¹³ Kate Jones

¹⁴ _____

¹⁵ Thomas Papenbrock

¹⁶ _____

¹⁷ Soren Soreson

¹⁸

Accepted for the Council:

¹⁹
²⁰

Carolyn R. Hodges

²¹

Vice Provost and Dean of the Graduate School

²² To the Graduate Council:
²³ I am submitting herewith a thesis written by Jason Bane entitled “The EMC Effect
²⁴ in A=3 Nuclei.” I have examined the final electronic copy of this thesis for form and
²⁵ content and recommend that it be accepted in partial fulfillment of the requirements
²⁶ for the degree of Doctor of Philosophy, with a major in Nuclear Physics.

²⁷ Nadia Fomin, Major Professor

²⁸ We have read this thesis
²⁹ and recommend its acceptance:

³⁰ Jamie Coble

³¹ _____
³²

³³ Kate Jones

³⁴ _____
³⁵

³⁶ Thomas Papenbrock

³⁷ _____
³⁸

³⁹ Soren Soreson

⁴⁰ _____
⁴¹

⁴² Accepted for the Council:

⁴³
⁴⁴ Carolyn R. Hodges

⁴⁵ _____
⁴⁶

⁴⁷ Vice Provost and Dean of the Graduate School

⁴⁸ (Original signatures are on file with official student records.)

49

The EMC Effect in A=3 Nuclei

50

A Thesis Presented for

51

The Doctor of Philosophy

52

Degree

53

The University of Tennessee, Knoxville

54

Jason Bane

55

May 2018

⁵⁶

© by Jason Bane, 2018

⁵⁷

All Rights Reserved.

⁵⁸ Contents

⁵⁹	List of Tables	v
⁶⁰	List of Figures	vi
⁶¹	1 Introduction	1
⁶²	1.1 Electron scattering	2
⁶³	1.1.1 Deep inelastic scattering	5
⁶⁴	1.2 EMC Effect	6
⁶⁵	1.3 MARATHON	9
⁶⁶	2 Experimental Setup	10
⁶⁷	2.1 Thomas Jefferson Lab	10
⁶⁸	2.1.1 CEBAF	10
⁶⁹	2.1.2 Hall A	12
⁷⁰	2.2 Target	17
⁷¹	2.3 High Resolution Spectrometers	19
⁷²	2.3.1 Vertical Drift Chambers	20
⁷³	2.3.2 Scintillators	22
⁷⁴	2.3.3 Cherenkov	22
⁷⁵	2.3.4 Shower Calorimeter	22
⁷⁶	2.3.5 Pion Rejector	22
⁷⁷	2.3.6 FPP Chambers	22

78	2.4 Trigger Setup	22
79	2.5 DAQ - Data Acquisition System	22
80	2.6 Kinematic Settings	22
81	3 Calibration	23
82	3.1 Beam Line	23
83	4 Data Analysis	26
84	5 Results	27
85	6 Simulation	28
86	6.1 Investigation	28
87	6.2 Transformation	29
88	6.3 Results	31
89	7 Conclusion	34
90	Bibliography	35

₉₁ **List of Tables**

₉₂ List of Figures

₉₃ 1.1	Simple Feynman diagram of an electron scattering from a proton [7].	3
₉₄ 1.2	Graph of the ratio of A/D structure functions vs x for Carbon [10].	7
₉₅ 1.3	EMC effect from EMC, SLAC, and BCDMS [17]	8
₉₆ 1.4	Graph of the ratio of A/D structure functions vs x for Carbon [10].	9
₉₇ 2.1	Schematic Layout of CEBAF.	11
₉₈ 2.2	A 3D drawing of Hall A.	12
₉₉ 2.3	A schematic layout of the beam line in Hall. [1]	13
₁₀₀ 2.4	BPM design diagram, from JLab instrumentation group. Beam direction is from left to right [23].	14
₁₀₂ 2.5	BPM design diagram, looking down the beam line[23].	14
₁₀₃ 2.6	Hall A Current Monitor components [4].	16
₁₀₄ 2.7	Target Images	18
₁₀₅ 2.8	A side view of a HRS [1].	20
₁₀₆ 2.9	A view of both the left(top) and right(bottom) detector stacks inside the left and right HRS [1].	21
₁₀₈ 2.10	A sketch of the two VDC planes in the HRSs with a particle traveling through the detector at 45° .[6].	22
₁₁₀ 3.1	A schematic layout of a harp fork [23]	24
₁₁₁ 3.2	The X and Y position for a Bulls eye scan for BPM calibration.	25

112	6.1 Example of the electron beam(red) with a energy of 2.5 GeV and the	
113	proton(blue) with angle of 45° in respect to the electron and with a	
114	momentum of 0.5 GeV/c.	29
115	6.2 Vector representations of the momentum for the incoming electron(red)	
116	and target proton(blue) with units of GeV for each phase of their	
117	transformations before scattering.	30
118	6.3 Vector representations of the momentum for the incoming electron(red)	
119	and target proton(blue) with units of GeV for each phase of their	
120	transformations after scattering).	32
121	6.4 Simulation results for fixed momentum protons. Three runs with	
122	unique proton momentum.	33

¹²³ **Chapter 1**

¹²⁴ **Introduction**

¹²⁵ Understanding the world around us is the goal of every scientist, from the chemist
¹²⁶ that experiments with the formation of atoms to the geologist exploring the process of
¹²⁷ rock formations. Nuclear physicists focus on studying the fundamental constituents
¹²⁸ of matter, the building blocks of nature. Physicist use scattering experiments at
¹²⁹ accelerator facilities, like CERN in Switzerland, DESY in Germany, BATES in
¹³⁰ Massachusetts, JLAB in Virginia, and many others, to study the protons and neutrons
¹³¹ and their constituents that make up a nucleus. These experiments allow physicists
¹³² to observe the internal structure of the nucleus and to investigate the interactions
¹³³ between the quarks and gluons. Many of the experiments are design to confirm a
¹³⁴ existing results while also expanding on unique ideas.

¹³⁵ In the last century, there have been numerous breakthroughs in the fields of nuclear
¹³⁶ and particle physics. Rutherford discovered the proton by bombarding light nuclei
¹³⁷ with alpha particles to produce



¹³⁸ This reaction allowed Rutherford to conclude that the Hydrogen nucleus was a
¹³⁹ constituent of an atomic nuclei [18]. In the late 1950s, experimental results published

140 by W. McAllister and R. Hofstadter exposed some of the eternal structure of the
141 proton [7, 15]. The European Muon Collaboration(EMC) produced results in the
142 early 1980s showing a differences between the internal structure of the deuterium
143 nucleus and Iron [20, 10]. The data received from scattering experiments using alpha
144 particles contain information about the target, the beam, and the interaction between
145 the two. Deciphering and analyzing this data can be convoluted because the cross-
146 section contains information about the internal structure of the target and the beam
147 along with the interaction and forces between the two [18].

148 1.1 Electron scattering

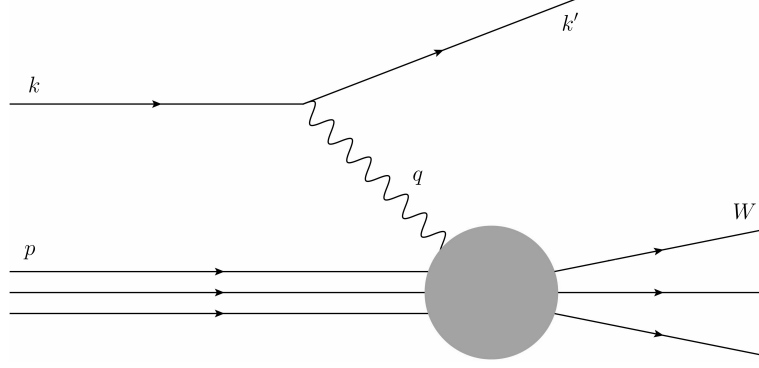
149 In order to remove some of the complexity in scattering experiments, one may
150 employ highly relativistic electrons. Electrons being point-like particles without any
151 internal structure allow the elimination of some of the analysis difficulties with using
152 alpha particles in scattering experiments due to their complex internal structure.
153 Electrons and the target nucleus, nucleon, or quarks interact via the exchange of
154 a virtual photon. Using quantum electrodynamics (QED), these interactions can
155 accurately be described by the well known electromagnetic interaction. Higher order
156 terms of this process contribute very little due to the coupling constant $\alpha \approx 1/137$,
157 being much smaller than one.

158 Figure 1.1 represents an electron scattering from a proton. The incoming or incident
159 electron's four-momentum is described as $k = (E, \vec{k})$ and the scattering electron's four-
160 momentum is represented by $k' = (E', \vec{k}')$. The exchange of the virtual photon in this
161 electromagnetic interaction is defined by the four-momentum transfer q :

$$Q^2 \equiv -q^2 = 4EE' \sin^2(\theta/2). \quad (1.2)$$

₁₆₂ In equation 1.2, E and E' are the electron energy before and after the scattering
₁₆₃ interaction. Theta is the angle that describes the deflection of E' from the electron's
₁₆₄ original path.

Figure 1.1: Simple Feynman diagram of an electron scattering from a proton [7].



₁₆₅ Along with Q^2 , the variables ν , W , and x_B are used to narrate the evolution of the
₁₆₆ electron scattering process. ν , defined as $p \cdot q/M$. In the rest frame of the target, ν
₁₆₇ can be described by:

$$\nu = E - E'. \quad (1.3)$$

₁₆₈ Simply, ν is the magnitude of energy loss by the electron during the scattering
₁₆₉ interaction. The invariant mass of the system, W , defines the hadronic state produced
₁₇₀ by the scattering event.

$$W^2 \equiv (q + p)^2 = M^2 + 2M\nu - Q^2. \quad (1.4)$$

₁₇₁ A scattering event with the invariant mass equal to the square of the mass of the
₁₇₂ nucleon, (M^2), falls in the regime of elastic scattering. W above M^2 will transform
₁₇₃ the scattering interaction from an elastic scattering to inelastic scattering due to
₁₇₄ the excited state of the scattered byproduct. x_B , the Bjorken scaling variable is a
₁₇₅ dimensionless quantity that measures the inelastically of a scattering process. x_B is
₁₇₆ defined as: $x := \frac{Q^2}{2M\nu}$.

177 The intrinsic likelihood of an event with a certain Q^2 , ν , and W is defined by the
 178 scattering cross section. An electron scattering off of a target with a charge of $Z * e$
 179 can be described by the Rutherford cross-section. Povh et. al. details the Rutherford
 180 cross section as:

$$\left(\frac{d\sigma}{d\Omega} \right)_{Rutherford} = \frac{(zZe^2)^2}{(4\pi\epsilon_0)^2 * (eE_{kin})^2 \sin^4(\theta/2)}. \quad (1.5)$$

181 The electron has a charge (ze) and kinetic energy of E_{kin} [18]. However in the early
 182 1920s, German physicists Stern and Gerlach performed an experiment that confirmed
 183 the presence of electron angular momentum. Later a discovery of electron spin was
 184 made by Uhlenbeck and Goudsmit. The Rutherford cross-section neglects the spin
 185 of the electron and the target. The Mott cross-section is the evolved version of the
 186 Rutherford cross-section. It has been modified to include the intrinsic spin of the
 187 target and electron. The Mott cross-section can be scribed as:

$$\left(\frac{d\sigma}{d\Omega} \right)_{Mott} = \frac{4Z^2\alpha^2(\hbar c)^2 E'^2}{|\mathbf{q}_c|^4} \cos^2(\theta/2)[12, 18]. \quad (1.6)$$

188 When the results from actual scattering experiments of electrons off nuclei or the
 189 nucleons located inside, there is an agreement between the measured cross section and
 190 the theoretical Mott cross-section when in the limit of $|\mathbf{q}| \rightarrow 0$. As $|\mathbf{q}|$ climbs furtherer
 191 from zero, the experimentally measured cross sections systematically decrease [18].
 192 Increasing the $|\mathbf{q}|$ of an interaction reduces the size of the wavelength of the virtual
 193 photon that mediates the electromagnetic interaction and increasing the resolution.
 194 The wavelength of this virtual photon is inversely proportional to $|\mathbf{q}|$, the amount of
 195 momentum transferred in an electron scattering interaction. The relationship between
 196 the wavelength and $|\mathbf{q}|$ can be described by the following: $\lambda = \frac{\hbar}{|\mathbf{q}|}$ [18]. Increasing the
 197 amount of momentum transferred in an electromagnetic reaction allows one to study
 198 deeper into the nucleus.

199 Studying the internal structure of a nucleus with the electromagnetic interaction
 200 requires increasing the momentum transferred. Pushing $|\mathbf{q}|$ to be comparable with the
 201 mass of a nucleon adds more complexity to the details of the scattering interaction.
 202 At the appropriate levels of $|\mathbf{q}|$ to study the nucleons in the nucleus, the Mott cross-
 203 section equation requires modifications to include additional factors that incorporate
 204 information about the target. The Rosenbluth formula is based on the Mott
 205 cross section and embraces target recoil, magnetic moment, and charge and current
 206 distributions. Povh writes the Rosenbluth formula as:

$$\left(\frac{d\sigma}{d\Omega} \right) = \left(\frac{d\sigma}{d\Omega} \right)_{Mott} * \left[\frac{G_E^2(Q^2) + \tau G_M^2(Q^2)}{1 + \tau} + 2\tau G_M^2(Q^2) \tan^2 \frac{\theta}{2} \right]. \quad (1.7)$$

207 Equation 1.7 contains $G_E^2(Q^2)$ and $G_M^2(Q^2)$, the electric and magnetic form factors. τ
 208 is used in the Rosenbluth formalism to account for the magnetic moment of a nucleon
 209 and is defined as: $\tau = \frac{Q^2}{4M^2c^2}$ [18]. In the general case of electron scattering off of a free
 210 proton or neutron elastically, the scattered energy of the electron will be a function
 211 of the incident electron's energy and the scattered angle of the electron, shown in the
 212 following equation.

$$E' = \frac{E}{1 + \frac{E}{Mc^2}(1 - \cos\theta)} \quad (1.8)$$

213 1.1.1 Deep inelastic scattering

214 The first generation of electron scattering experiments achieving a significantly
 215 large $|\mathbf{q}|$ used a linear accelerator with a 25 GeV maximum beam energy, and
 216 following generations increased the total interaction energy to substantially higher
 217 thresholds. At these high incident beam energies, individual resonances cannot be
 218 separated in the invariant mass spectrum above 2.5 GeV. Observations made into
 219 this convoluted invariant mass spectrum has shown that many strongly interacting
 220 particles are produced, known as hadrons. Scattering interactions that generate
 221 these hadrons are title inelastic scattering. Inelastic scattering events contain the
 222 possibility of conceiving additional resultants and increase the complexity of the

scattering interaction. Due to the increase in complexity, an additional degree of freedom has to be included into the scattering cross section. This can be done by slightly modifying the Rosenbluth formula to include the inelastic scattering structure functions $W_1(Q^2, \nu)$ and $W_2(Q^2, \nu)$. This modification is shown in equation, 1.9.

$$\frac{d^2\sigma}{d\Omega dE'} = \left(\frac{d\sigma}{d\Omega} \right)_{Mott} \left[W_2(Q^2, \nu) + 2W_1(Q^2, \nu) \tan^2 \frac{\theta}{2} \right] \quad (1.9)$$

Inelastic scattering events occur when the wavelength of the virtual photon is comparable to the radius of the struck nucleon or when $Q^2 R^2 \lesssim 1$. When $Q^2 R^2 \gtrsim 1$, the probe may interact with the charge constituents deep within the nucleon. When the scattering happens off fundamental parts of the proton or neutron, the scattering process is titled deep inelastic scattering(DIS).

[21] [13]

1.2 EMC Effect

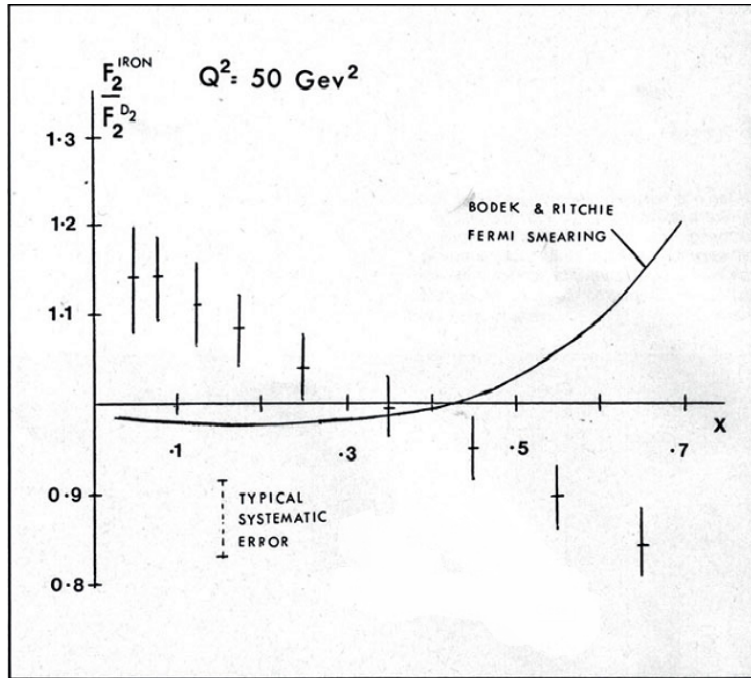
The European Muon Collaboration (EMC) performed a deep inelastic measurement with 120-280 GeV muons on iron and deuteron targets [14]. The EMC extracted A/D structure function ratios versus the Bjorken scaling variable, x . The relationship originally expected by the EMC contained the sum of the structure functions of each nucleon in a nucleus. Each nucleus has a certain number of neutrons (N) and a amount of protons (Z). The expected structure function for a nucleus could be written as:

$$F_A = N F_2^N + Z F_2^P. \quad (1.10)$$

The EMC compared the extracted structure functions from iron and deuterium. Their results are shown in Figure 1.2. The $\frac{A}{D}$ structure function ratio showed an unexpected downward slope. This phenomenon was titled the EMC effect. This finding demonstrated to the EMC that their understanding of the nucleus

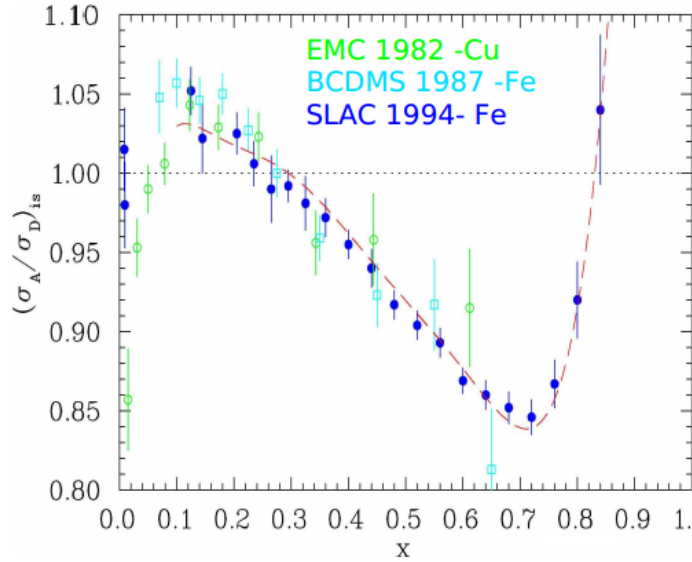
²⁴⁴ was incorrect. A nucleon's structure function and thereby, the constituent quark distributions may be altered by the nucleus.

Figure 1.2: Graph of the ratio of A/D structure functions vs x for Carbon [10].



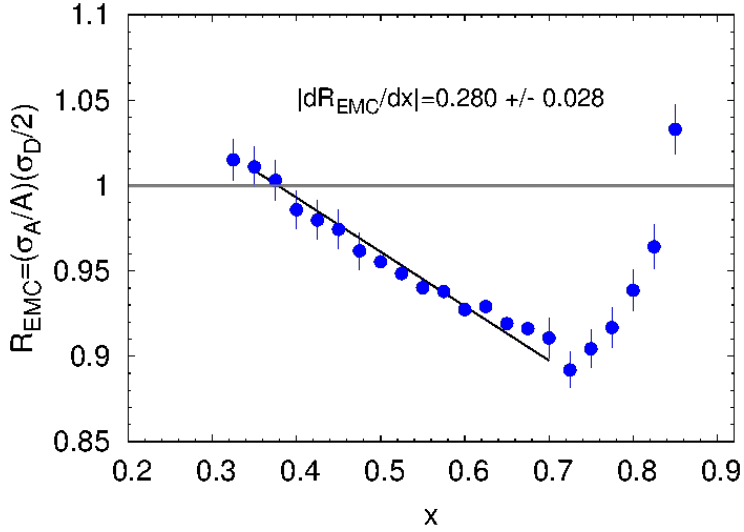
258 of the A/D ratios. These models can contain traditional nuclear physics effects like
 259 momentum distribution or pion-charge contributions. Some models also describe the
 260 EMC effect through quark momentum distribution or modification of the internal
 261 structure [17, 5, 2, 8, 9]. However, no single model has provided a complete picture
 262 of the possible underlying physics. Precise data from Jlab's E03-103 experiment has
 263 revitalized this research. This experiment focused on precision measurements in light
 264 nuclei and added ${}^3\text{He}$ as a target nucleus. Instead of taking the A/D ratio at a
 265 certain x -value to be the magnitude of the EMC effect, this analysis looked at the
 266 slope instead. This eliminated sensitivity to normalization uncertainties.

Figure 1.3: EMC effect from EMC, SLAC, and BCDMS [17]



267 In Figure , ${}^9\text{Be}$ was found not to follow the previously observed scaling with
 268 nuclear density. This result from Jefferson Lab determined that the previous idea
 269 of a dependence on A or nuclear density in the EMC effect to be incorrect [20]. This
 270 result spawned a drive to determine another explanation for the EMC effect and
 271 understand what clue the ${}^9\text{Be}$ outlier was providing. The structure of this nucleus
 272 is made up of two high-density alpha particles and a single neutron [3]. The regions

Figure 1.4: Graph of the ratio of A/D structure functions vs x for Carbon [10].



of higher density that are contained in a comparatively large volume may be able to explain why ${}^9\text{Be}$ does not follow the expected trend. This suggests that the EMC effect could be a function of local nuclear density [20].

1.3 MARATHON

Experiment E12-010-102, MARATHON (MeAsurement of the $F2^n/F_2^p, d/u$ Ratios and A=3 EMC Effect in Deep Inelastic Electron Scattering Off the Tritium and Helium MirOr Nuclei), will use deep inelastic scattering off of the mirror nuclei ${}^3\text{H}$ and ${}^3\text{He}$ to measure the EMC effect for both ${}^3\text{H}$ and ${}^3\text{He}$, to determine the ratio of the neutron to proton inelastic structure functions, and to find the ratio of the down to up quark distributions in the nucleon.

283 **Chapter 2**

284 **Experimental Setup**

285 **2.1 Thomas Jefferson Lab**

286 Thomas Jefferson Lab (Jlab) in Newport News, Virginia hosted the MARATHON
287 experiment in the Fall of 2017 and Spring of 2018. Jlab uses support from the U.S.
288 Department of Energy(DOE) and the state of Virgina to complete the lab's mission of
289 delivering productive research by exploring the atomic nucleus and its fundamental
290 constituents, including precise tests of their interactions. Along with applying an
291 advanced particle accelerator, particle detectors and other technologies to develop
292 new basic research capabilities and to address the challenges of a modern society.

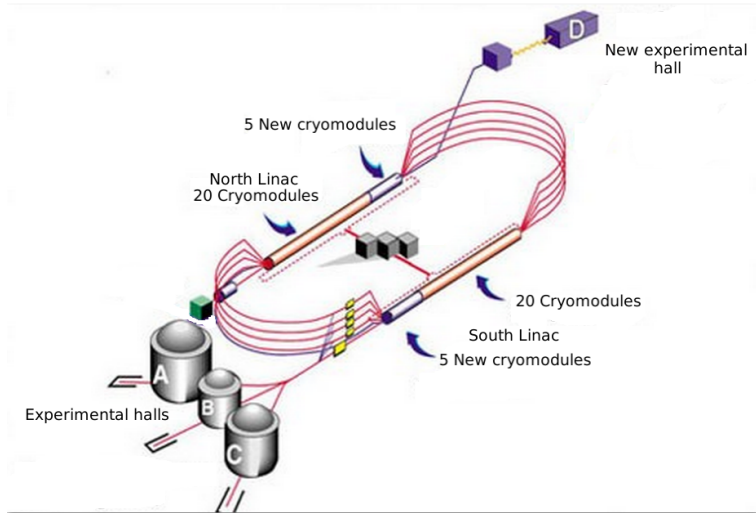
293 **2.1.1 CEBAF**

294 The Continuous Electron Beam Accelerator Facility (CEBAF) was recently
295 upgraded to a 12 GeV accelerator, upgrading it to be able to supply a 11 GeV beam
296 of continuous electrons of up to $200 \mu\text{A}$ of current to three experimental halls (A,B,C)
297 and 12 GeV to the recently constructed hall D. After being accelerated to 45 MeV by
298 a polarized electron gun or a thermionic injector, the electrons are injected into the
299 North linear accelerator (LINAC), shown in figure 2.1. The polarized gun can supply
300 electrons with up to 80% polarization and the polarization direction can be controlled

301 by a wien filter. To ensure the level of polarization, a 5 MeV Mott polarimeter may
302 be used to measure the level of polarization[1].

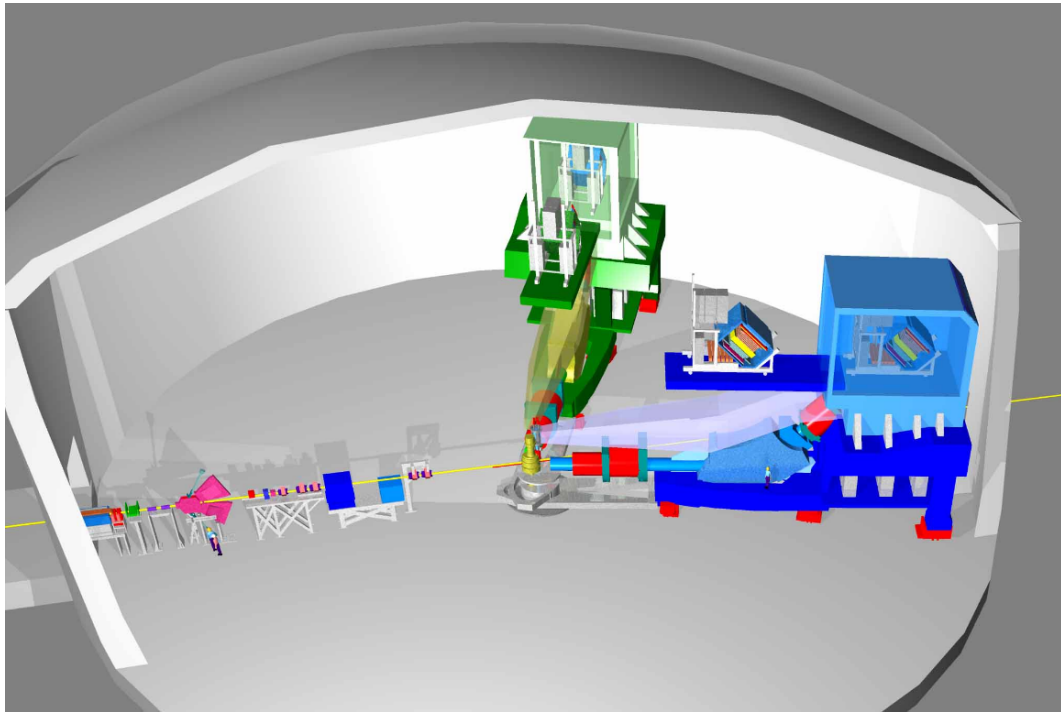
303 The electrons are conveyed through two LINACs and two bending arcs per complete
304 pass of the accelerator. Electrons traveling to Halls A, B, and C complete a maximum
305 of four and a half revolutions around the accelerator. Electrons going to all D travel
306 through the north LINAC for an extra boost. These particles receive approximately
307 2.2 GeV in energy for each cycle through the accelerator. The radio frequency (RF)
308 cavities in each LINAC use an oscillating electromagnetic field to supply a force to
309 accelerate the passing electrons. These Niobium RF cavities are cooled to 2 K in
310 order to create conditions that allow the cavities to be superconducting [1].

Figure 2.1: Schematic Layout of CEBAF.



₃₁₁ **2.1.2 Hall A**

Figure 2.2: A 3D drawing of Hall A.

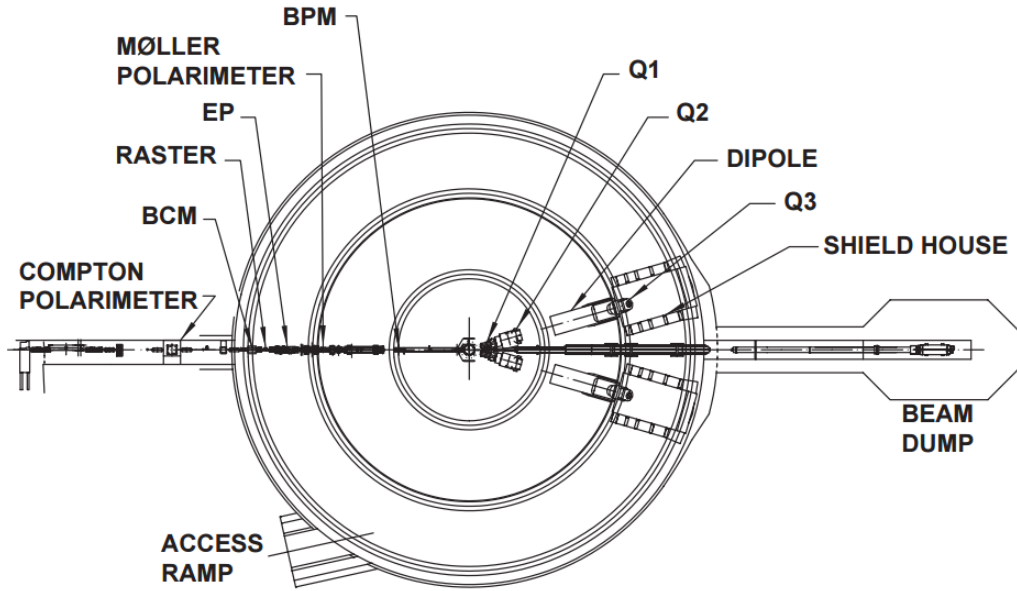


₃₁₂ The experimental Hall A and the scientific equipment used were designed for
₃₁₃ detailed investigations of the internal structure of nuclei. Two high resolution
₃₁₄ spectrometers in Hall A use the inclusive (e,e') and exclusive $(e,e' p)$ reactions to gain
₃₁₅ a greater understanding of the structure of the nucleus. Completing detailed studies
₃₁₆ with high resolution and extreme accuracy requires knowing the beam position, size,
₃₁₇ energy, current, direction, and polarization when the beam strikes the target. The
₃₁₈ instrumentation used in the precise measurement of these quantities in Hall A are
₃₁₉ shown in figure 2.3 [1].

₃₂₀ A pair of Beam Position Monitors(BPM)s are used to measure the relative beam
₃₂₁ position without affecting the beam. The two Hall A BPMs are located at 7.524 m
₃₂₂ and 1.286 m away from the target. Using the standard difference-over-sum technique,
₃₂₃ the relative beam position is determined with an accuracy of $100 \mu\text{m}$ with a beam

324 current of at least $1 \mu\text{A}$ [1]. The BPMs' positional data is recorded in two ways.
 325 Every second of beam time, the beam position average over 0.3 seconds is logged
 326 into the Experimental Physics and Industrial Control System (EPICS) database.
 327 The BPMs also transmit data event-by-event to the CEBAF online Data Acquisition
 328 system(CODA).

Figure 2.3: A schematic layout of the beam line in Hall. [1]



329 The main beam line components of the BPMs consist of four open-ended antennas.
 330 Figure 2.4 shows a BPM chamber and figure 2.5 shows the layout of the four antennas
 331 as you look down the beam line. In this chamber, the design of three of the four
 332 antennas can be seen. The antennas are titled u_+ , u_- and v_+ , v_- . The antennas
 333 receive an induced signal as electrons pass to determine the beam position in the
 334 u and v directions. The direction of the beam is determined by using the two
 335 BPMs in conjunction with timing information provided. The accuracy of the BPMs
 336 requires an absolute measurement of the electron beam's position to calibrate the
 337 BPMs and a internal input oscillation measurement names twiddle to supply BPM
 338 signal coefficients. [19, 23].

Figure 2.4: BPM design diagram, from JLab instrumentation group. Beam direction is from left to right [23].

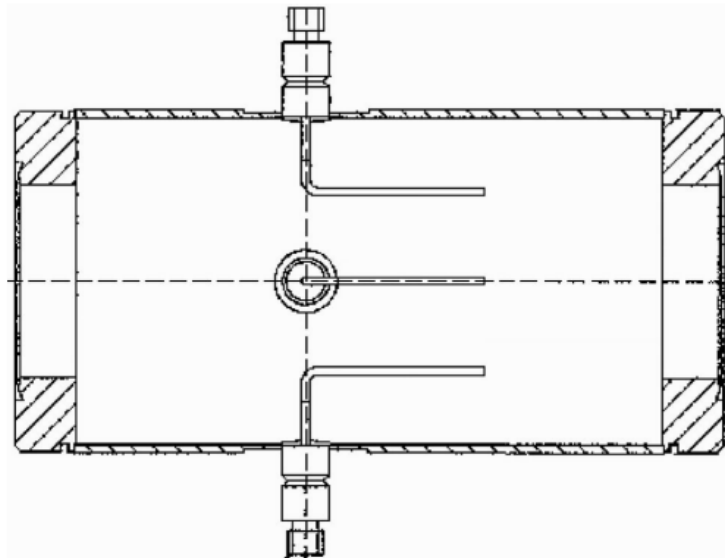
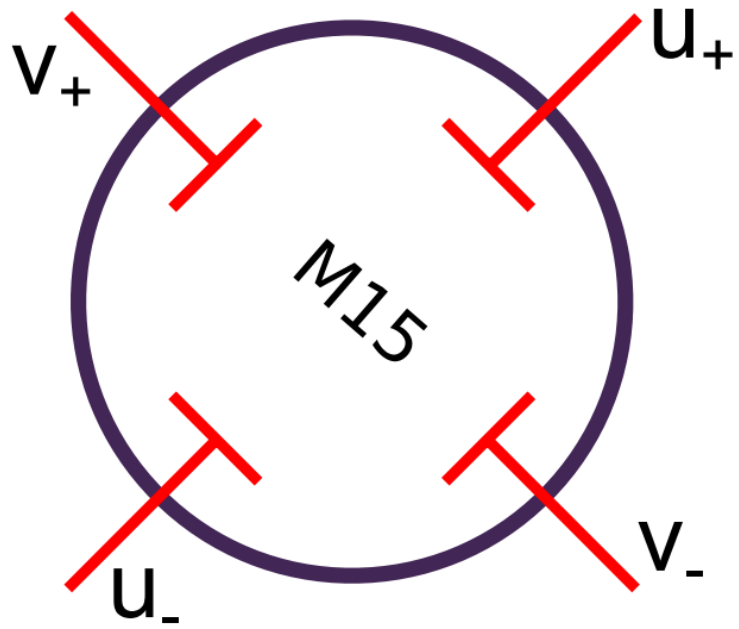


Figure 2.5: BPM design diagram, looking down the beam line[23].



339 Damage to a target system from intense beam can cause extreme fluctuations in
340 the target's temperature and density. A raster was used to counteract the damage

341 caused by a focused beam. The raster used two magnetic fields produced by two
342 dipoles to spread the electron beam out. This produces a large rectangle interaction
343 area on the front face of the target container. A triangle wave of 25 kHz was used to
344 control the coils of the dipole magnets. The raster systems are located \approx 17 meters
345 before the target chamber (upstream of the target[23]). The rasters position can be
346 seen in figure 2.2. Safety constraints administrated by the target group at JLAB
347 limited the minimum size of the raster spot for the MARATHON experiment to two
348 millimeters by two millimeters. This limit was installed has a safety concern for the
349 tritium target.

350 The Hall A raster system consists of four dipoles. Two dipoles produce magnetic
351 fields in the horizontal direction of the lab frame and two in the vertical. The upstream
352 raster and downstream rasters include one vertical and one horizontal dipole. The
353 relative change in position of the incoming electrons are controlled by the current
354 supplied to the dipoles. In order to obtain the change in beam position due to the
355 rasters, a calibration between the raster current and measured beam position were
356 obtained.

357 The electron beam energy is located in many of the equations used in an electron
358 scattering experiment. This can cause a noticeable increase in systematic error if the
359 beam energy measurement is not made precisely. At JLAB for the MARATHON
360 experiment, the beam energy was measured in two ways. In Hall A, the beam energy
361 was measured by using the (e,e/p) method. On the beam line, 17 meters upstream
362 from the target an ep scattering chamber is located. The beam was directed into the
363 target containing a rotating 10-30 μ m thick tape of CH_2 . The scattering angle of the
364 electron and the recoil angle of the proton are used to determine the beam energy
365 using equation 2.1. Where M_p is the mass of the proton and θ_p, θ_e are the scattered

³⁶⁶ angle of the proton, electron respectively.

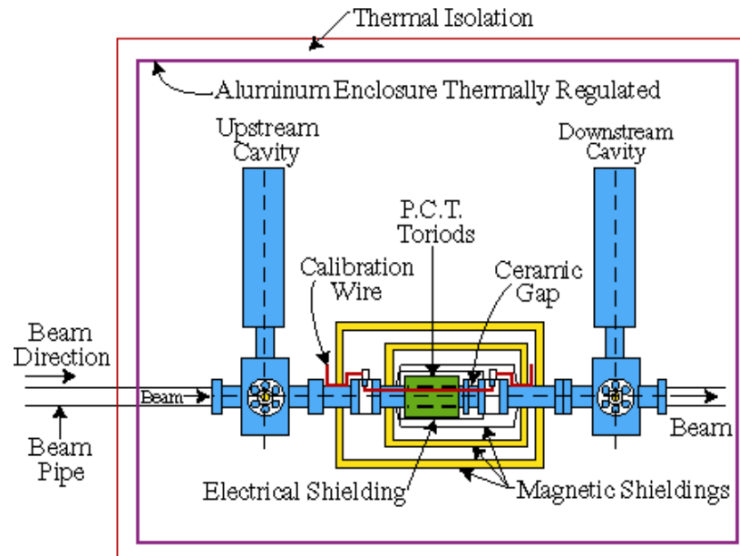
$$E = Mp \frac{\cos\theta_e + \frac{\sin\theta_e}{\tan\theta_p} - 1}{1 - \cos\theta_e} \quad (2.1)$$

³⁶⁷ The beam energy was also measured using the ark measurement method [7]. This
³⁶⁸ method uses changes in beam position and precise measurements of the magnetic
³⁶⁹ fields around the beam line to determine the energy of the electron beam. The angle
³⁷⁰ at which the electrons are bent through is related to the momentum of the electrons,

$$p = k \frac{\int \vec{B} \cdot d\vec{l}}{\theta}. \quad (2.2)$$

³⁷¹ In equation 2.2, p is the momentum of the electrons, θ is the bend angle, and \vec{B}
³⁷² is the magnetic field the electron experiences. Then using the momentum of the
³⁷³ electron, the energy of the beam can be extracted. The error on the beam energy
³⁷⁴ measurement is $\delta E/E \approx 2 * 10^{-4}$ [22, 7]. The MARATHON experiment used both
³⁷⁵ methods to accurately determine the electron beam energy.

Figure 2.6: Hall A Current Monitor components [4].



376 The main process of measuring the scattering yield for a calculation of a cross
377 section looks at finding the ratio of the number of electrons scattered to the number
378 of electrons sent. In order to accurately determine the number of electrons sent to
379 scatter with our target system, Hall A use a highly accurate and non-invasive beam
380 current monitor(BCM). The Hall A BCM has an absolute accuracy of 0.2 percent
381 as long as the current is between 1 and 180 μ A. The BCM used in Hall A consists of
382 three main components: a Parametric Current Transformer (PCT) and two pill box
383 cavities. Figure 2.6 shows the components in the Hall A BCM. The BCM produces
384 an RF signal that is proportional to the beam current. An 10 kHz down converter,
385 RMS-to-DC converter, voltage-to-Frequency converter, and a scaler are used to inject
386 the current signal into the Hall A DAQ. Proportionality constants are determined in
387 the calibration process to correctly integrate the charge for a given amount of beam
388 current[4]. Continue after the initial beam line components, an electron will enter
389 into the target chamber, housing the target system.

390 2.2 Target

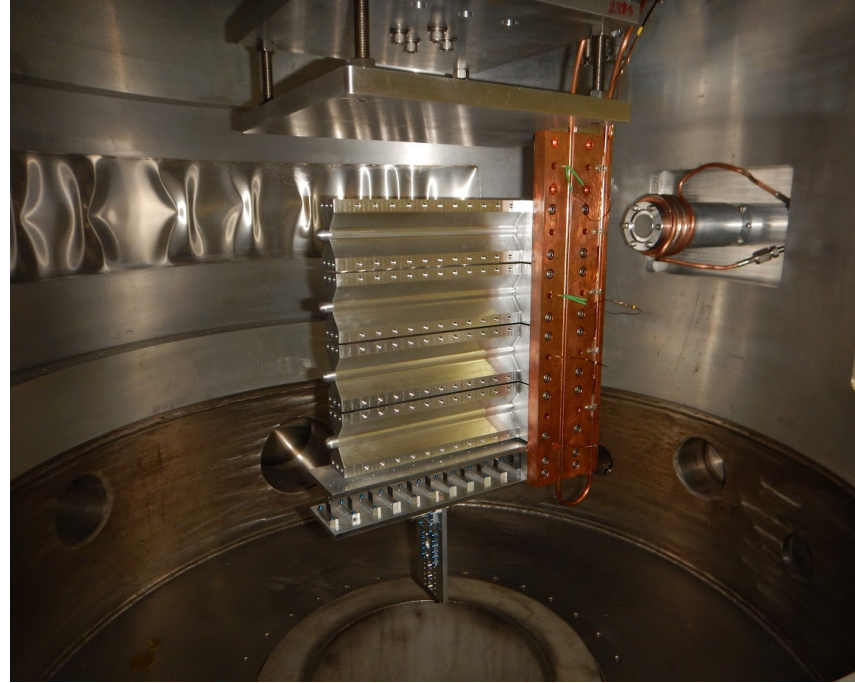
391 The Hall A Tritium Target(HATT) system was used for the Tritium run group of
392 experiments. The HATT target chamber was repurposed from a previously used cryo-
393 target chamber in order to reduce the financial cost of designing a new target chamber.
394 The refurbishing of the cryo-target chamber consisted of adding in new safety features
395 to prevent and mitigate a tritium leak. A 4 inch long collimator with an inner diameter
396 of 0.4 inch was added inside of the target chamber but upstream of the target ladder
397 to prevent the beam from striking the thin side wall of the aluminum cell. In case of
398 a tritium leak in the target chamber, an exhaust system was installed to control the
399 amount of tritium exposed to the Hall.[16] Figure 2.7 shows the HATT system with
400 the target ladder in the home position and the scattering windows removed. A picture
401 of the HATT ladder installed in the HATT system is shown if figure 2.7. The ladder
402 contains both gaseous cells and solid targets. The MARATHON experiment had five

Figure 2.7: Target Images

(a) A image of the HATT. [11]



(b) Image of the Hall A Tritium Target Ladder. [11]



403 gas cells. The top four of the gas cells were filled with tritium, deuterium, hydrogen,
404 and $^3\text{helium}$, from top to bottom respectively. Due to safety restricts the tritium
405 cell was not installed until the HATT system could be closed. The bottom most
406 cell was left empty, to complete end cap subtractions. The lower half of the target
407 ladder contains the solid targets used during the MARATHON experiment. Listed
408 from top to bottom, the solid targets used were a pair of thick aluminum foils, carbon
409 multifoil, single carbon foil, and a carbon foil with a 2mm diameter hole. The thick
410 Al foils were used to aid the target window background subtraction. The multifoil
411 target also know has the optics target was used to calibrate the z-axis reconstruction
412 of the optics matrix. The single carbon foil and carbon hole were used to calibrate
413 the BPMs and rasters and to determine the off set of the central line of the detector.

414 2.3 High Resolution Spectrometers

415 Electrons that successfully scatter from the target may end up in either of the two
416 HRSs(High Resolution Spectrometers). The HRSs were designed to detect charged
417 particles with a high degree of precision. In order to achieve a high level of resolution
418 in momentum and angle, the HRSs were designed with a magnet configuration of
419 QQD_nQ (quadrupole, quadrupole, dipole, and quadrupole). The vertical bending
420 dipole provides the field required to transport the scattered particles through the
421 45° bending angle to the detector hut. A drawing of an HRS can be seen in
422 figure 2.8. The first quadrupole(Q1) focuses the incoming electrons in the vertical
423 plane. The following two quadrupoles (Q2 and Q3 provide transverse focusing. This
424 optical design allows the use of extended gas targets with no substantial loss in solid
425 angle[1]. The spectrometers were designed to perform various functions which include:
426 triggering the data acquisition system (DAQ) when certain requirements are met,
427 gathering the position and direction of individual particles to reconstruct a track,
428 provide precise timing information for time of flight calculations, and identify many
429 different particle types that pass through the detector system. In order for both
430 the Left HRS (LHRS) and Right HRS (RHRS) to complete the required task, they
431 contain a myriad of detectors. The HRSs use drift chambers, scintillators, cerenkov
432 detectors, and shower calorimeters. Both the Left and Right HRSs contain two planes
433 of scintillators to function has the main trigger for the detector package. The vertical
434 drift chambers (VDC) that lay at the front of the detector in conjunction with the
435 Shower that lies in the back of the detector provide information for reconstructing the
436 particle tracks and precise timing. Particles are identified by the cerenkov, shower
437 calorimeters, and pion rejectors that are contained in the left or right HRS. The
438 layout of the individual detectors that make up the left and right detector package
439 are shown in figure 2.9 [1].

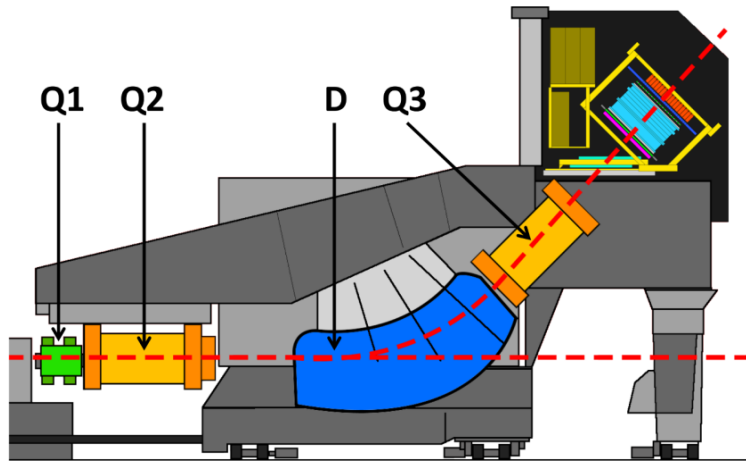


Figure 2.8: A side view of a HRS [1].

440 2.3.1 Vertical Drift Chambers

441 Each of the spectrometers housed in Hall A contains a vertical drift chamber(VDC).
 442 Each VDC contains two planes of crossing sense wires. Shown in figure 2.10, the two
 443 planes of the VDC lie a distance of 0.335m apart [6]. The lower plane of the VDC
 444 is positioned at the approximate focal plane of the HRS and lies in the horizontal
 445 plane of the Hall A coordinate system. The sense wires located in the VDCs cross
 446 orthogonally. They are offset by 45° in respect to the dispersive and non-dispersive
 447 directions.

448 [6]

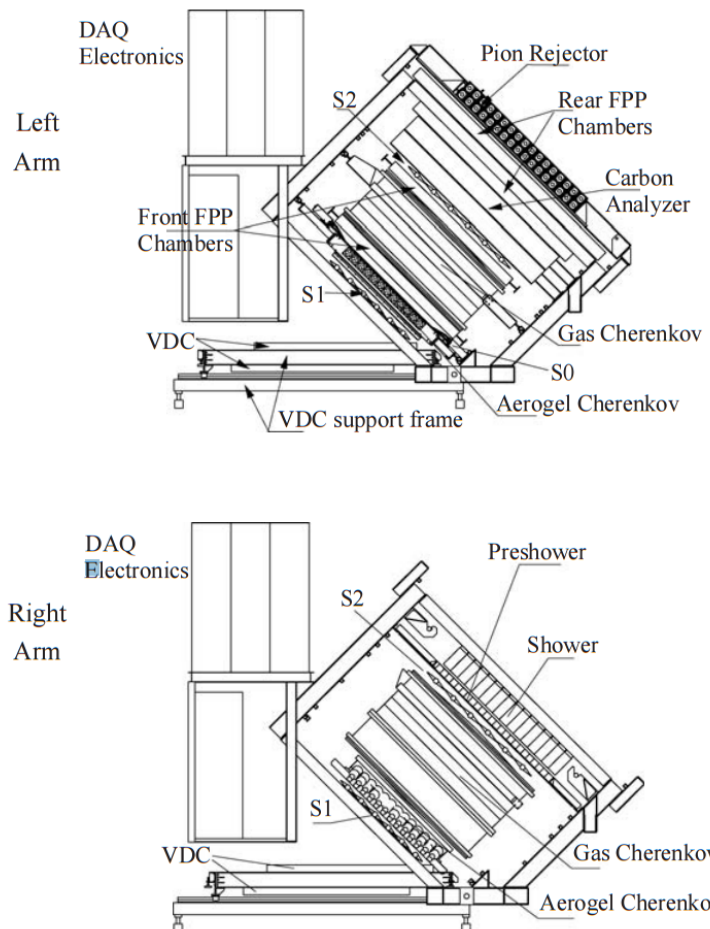


Figure 2.9: A view of both the left (top) and right (bottom) detector stacks inside the left and right HRS [1].

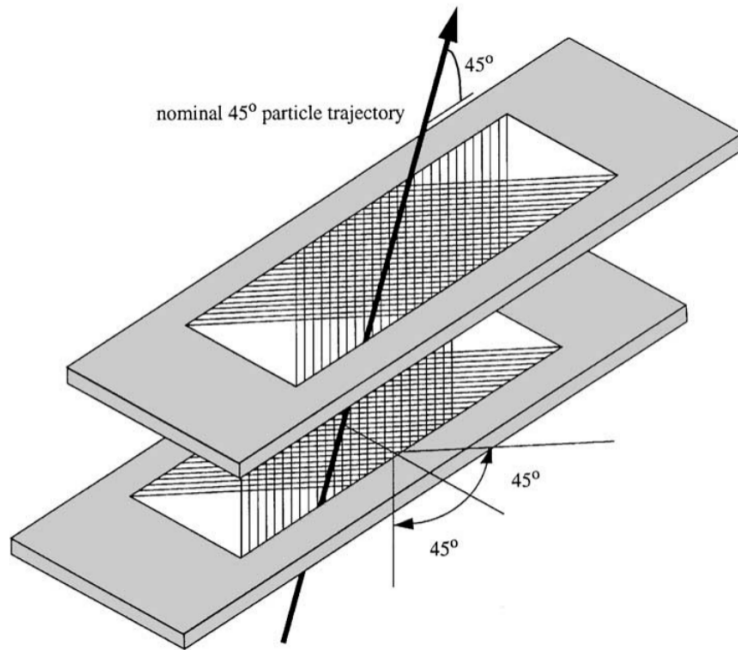


Figure 2.10: A sketch of the two VDC planes in the HRSs with a particle traveling through the detector at 45° .[6].

449 **2.3.2 Scintillators**

450 **2.3.3 Cherenkov**

451 **2.3.4 Shower Calorimeter**

452 **2.3.5 Pion Rejector**

453 **2.3.6 FPP Chambers**

454 **2.4 Trigger Setup**

455 **2.5 DAQ - Data Acquisition System**

456 **2.6 Kinematic Settings**

457 **Chapter 3**

458 **Calibration**

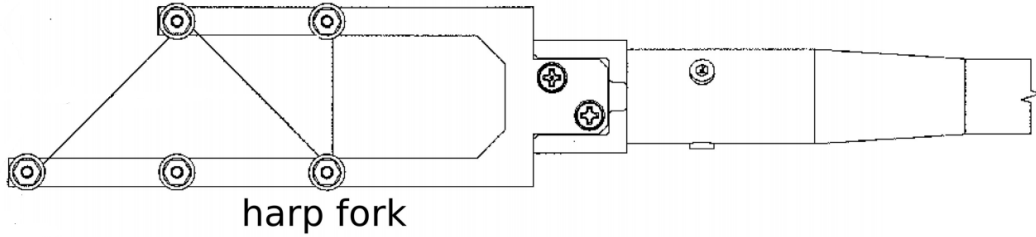
459 The information provided by the detectors originate through small changes in
460 current and voltage sent through the DAQ electronics. These signals are transformed
461 into useful information through calibration constants. The beam line elements and the
462 individual detector components were calibrate to supply highly precise and accurate
463 data.

464 **3.1 Beam Line**

465 The BPM signal coefficients are determined by a twiddle measurement. An RF
466 module attached to the BPM antennas is used to pass a signal out of each of the
467 antennas, one at a time. This will allow the determination of the conversion factor
468 for the BPM signal to relative beam position. Two harps were used to provide
469 the absolute measurement required for calibrating the BPMs. Figure 3.1 contains a
470 drawing of the harps used in Hall A. The harps were moved into the beam line when
471 calibration data is needed, but must be moved out for the production of experimental
472 data because the harp wires are intrusive to the beam operation. The harp forks are
473 aligned perpendicular to the beam line, to allow the harps to be moved in and out of
474 the beam line. Three different wires are used to determine the horizontal and vertical
475 position of the beam. Each wire has one of three orientations: vertical, sloped down

476 or sloped up. The two sloped wires are angled at 45° relative to the wire frame. As
 477 the harp fork is moved into the beam, the wires receive a signal as the beam interacts
 478 with the wires. The two sloped wires are used together to determine the vertical
 479 position of the beam. The vertical wire is used to determine the horizontal position
 480 of the beam [19, 23].

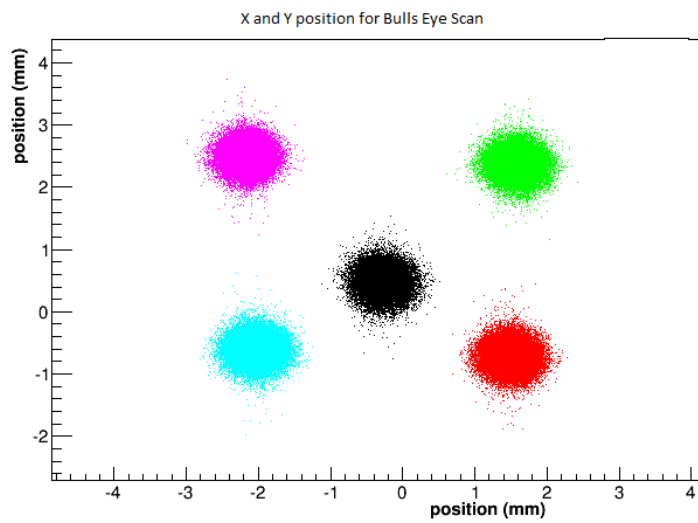
Figure 3.1: A schematic layout of a harp fork [23]



481 The location of the wires on the harp frame and the position of the harp fork
 482 were used to calculate the absolute beam position. The BPM calibration coefficients
 483 were determined by using a bulls eye scan, figure 3.2 shows an example of the five
 484 positions used to calculate the BPM calibration coefficients. The harp scan results
 485 are substituted into equation 3.1 for the X and Y positions. Using all five points and
 486 an R^2 regression technique, the coefficients can be determined with great accuracy.
 487 These highly accurate BPMs were crucial in reducing systematic error in the final
 488 results obtained from this experiment.

$$\begin{pmatrix} X_{position} \\ Y_{position} \end{pmatrix} = \begin{pmatrix} C(0, 0) & C(0, 1) \\ C(0, 0) & C(0, 1) \end{pmatrix} * \begin{pmatrix} X_{BPM} \\ Y_{BPM} \end{pmatrix} + \begin{pmatrix} X_{offset} \\ Y_{offset} \end{pmatrix} \quad (3.1)$$

Figure 3.2: The X and Y position for a Bulls eye scan for BPM calibration.



489 Chapter 4

490 Data Analysis

₄₉₁ Chapter 5

₄₉₂ Results

493 **Chapter 6**

494 **Simulation**

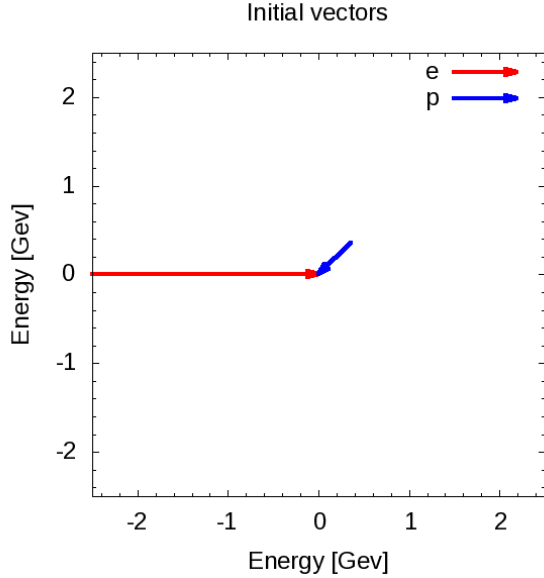
495 Nuclei are systems of nucleons that interact strongly. The characteristic scale for the
496 nucleons momentum is approximately the Fermi momentum, $k_F \approx 200 - 270 \text{ MeV}/c$
497 [9]. However because of the strongly repulsive nature of the nucleon-nucleon
498 interaction at short distances prevents two nucleons from laying in close proximately
499 to each other. This strong interaction demands the presence of high-momentum
500 components in the nuclear ground state wave function. A simulation was designed
501 to phenomenologically study the effect of these high-momentum components on the
502 nuclear EMC effect. This program was designed in two phases. The first phase used
503 simple elastic scattering and a single value for the targets momentum to investigate
504 overall effect of different target momentum on the yield in bins of x_B . The second
505 phase of the simulation was created to lay out the effect of using different momentum
506 distributions on the yield for the EMC effect region of x_B , 0.3 to 0.7.

507 **6.1 Investigation**

508 This simulation phenomenologically investigates the effect of a moving target on the
509 EMC effect by scattering a beam of electrons off of a moving proton. The target
510 protons are comprised of a directional vector of 0° to 360° in respect to the incoming
511 electron beam and a momentum between 0 and 1 GeV/c. Figure 6.1 contains a

512 possible event for the simulation. The electron approaches with 2.5 GeV of energy
513 and collides with a proton moving with a momentum of 0.5 GeV/c with an angle of
45° in respect to the electron trajectory.

Figure 6.1: Example of the electron beam(red) with a energy of 2.5 GeV and the proton(blue) with angle of 45° in respect to the electron and with a momentum of 0.5 GeV/c.



514
515 Using conservation of momentum and conservation of energy in elastic collisions,
516 this simulation calculates the final state of the electron and proton after the scattering
517 event by randomly selecting a scattered direction for the electron. The vector
518 representation of the scattered products are shown in figure 6.3a. In order to
519 make these calculations systematic and to study cross sections models the simulation
520 transform each event into the rest frame of the target before scattering.

521 6.2 Transformation

522 The Simulation completes a set of Lorentz invariant rotations and boost for each
523 event to transform the lab frame of the electron and proton collision into the rest
524 frame of the proton. First the simulation takes the initial proton and electron vectors

525 and rotates them to align the proton vector to the horizontal axis, shown in figure
 526 6.2b. This rotation uses the angle between the proton and the electron defined as λ .
 527 This allows for a straight forward calculations for the Lorentz factors β and γ and
 528 to boost into the rest frame of the target proton, figure 6.2c. Once in the boosted
 529 frame, the angle between the electron and the horizontal axis is defined as δ . Right
 530 before the simulation starts to calculate the scattered products, it completes one more
 531 rotation to align the electron vector with the horizontal axis, figure 6.2d, to make the
 532 scattering calculation systematic and unconditional.

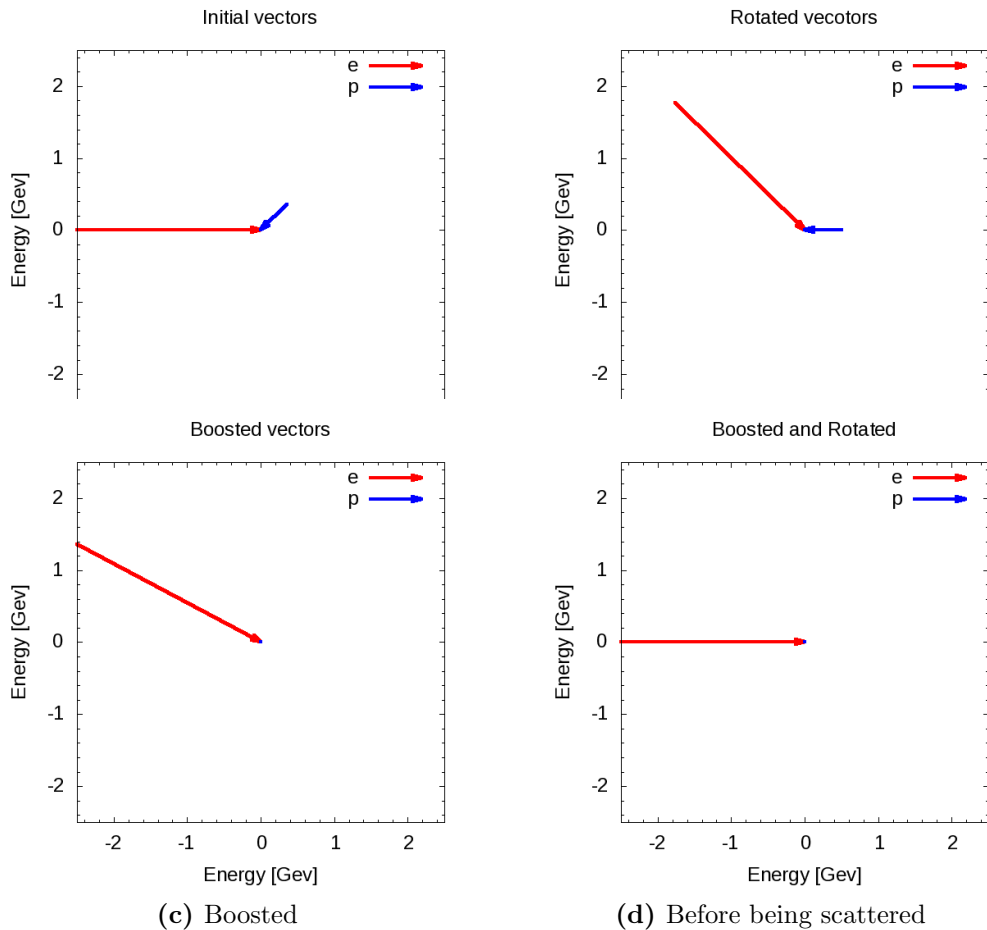


Figure 6.2: Vector representations of the momentum for the incoming electron(red) and target proton(blue) with units of GeV for each phase of their transformations before scattering.

533 In order to gain a more complete understanding of the scattering products, the
534 program completes a set of transformations to move from the rest frame of the target
535 proton to the beginning lab frame. After the simulation calculates the scattered
536 products it begins to transform back by beginning with a rotation by the angle δ ,
537 figure 6.3b. Followed by the inverse of the previously used Lorentz boost. The
538 last transformation, a rotation by λ , transforms the frame back into the lab frame.
539 A proton vector and electron vector in the lab frame are the final products of the
540 simulation. An image of the electron and proton vectors for each transformation can
541 be found in figure 6.3. These vectors allow for calculation of kinematic variables such
542 as Bjorken x and the four-momentum transfer (Q^2). This simulation will complete
543 these steps for many electron and proton combinations.

544 6.3 Results

545 This electron scattering simulation produced results for two stages. The firsts stage
546 used a fix proton momentum for each run to compare the yield in bins of x_B . Figure
547 6.4 shows the results for three different runs, each having a unique fixed proton
548 momentum. The red histogram represents a run with a proton momentum of 0 Gev/c.
549 The result is an elastic peak at x_B of one. The blue histogram contains the results
550 having a fixed proton momentum of 0.25 GeV/c. Increasing the initial momentum
551 of the proton spreads the events into two peaks. The scattering interactions that
552 form the peak above 1 x_B are produced by events were the proton's initial directional
553 vector are orientated towards the electron. The events that produce an x_B below
554 1 have a proton direction pointing away from the electron initially. Doubling the
555 proton's initial momentum from 0.25 GeV to 0.50 GeV causes these peaks two spread
556 out furtherer in x_B .

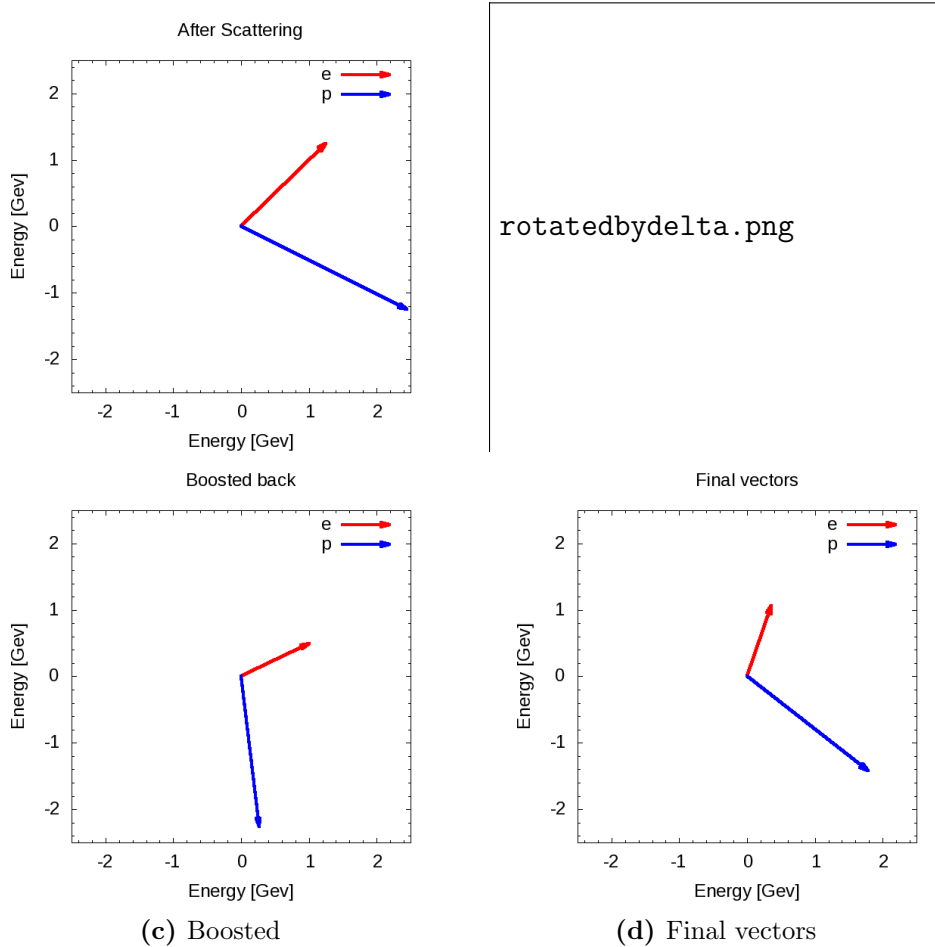
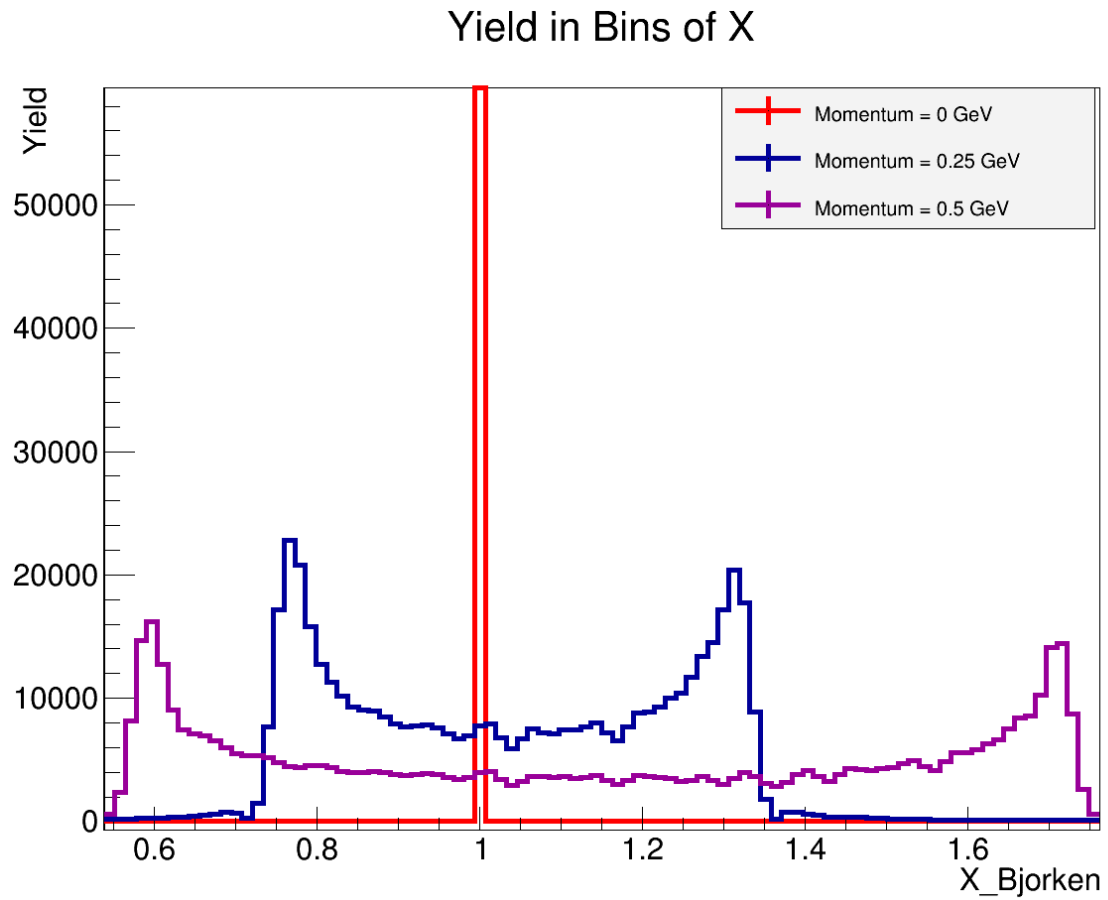


Figure 6.3: Vector representations of the momentum for the incoming electron(red) and target proton(blue) with units of GeV for each phase of their transformations after scattering).

Figure 6.4: Simulation results for fixed momentum protons. Three runs with unique proton momentum.



557 Chapter 7

558 Conclusion

Bibliography

560 **Bibliography**

- 561 [1] J. Alcorn et al. Basic Instrumentation for Hall A at Jefferson Lab. *Nucl. Instrum.*
562 *Meth.*, A522:294–346, 2004. [vi](#), [11](#), [12](#), [13](#), [19](#), [20](#), [21](#)
- 563 [2] John Arrington, Aji Daniel, Donal Day, Nadia Fomin, Dave Gaskell, and Patricia
564 Solvignon. A detailed study of the nuclear dependence of the EMC effect and
565 short-range correlations. *Phys. Rev.*, C86:065204, 2012. [8](#)
- 566 [3] A. Daniel, J. Arrington, and D. Gaskell. Measurements of the EMC effect in
567 few-body nuclei at large x. *AIP Conf. Proc.*, 1369:98–105, 2011. [8](#)
- 568 [4] J. Denard and J. Sahar. High accuracy beam current monitor system for cebaf’s
569 hall a. Chicago, 2001. Particle Accelerator Conference. [vi](#), [16](#), [17](#)
- 570 [5] J. Edelmann, G. Piller, Norbert Kaiser, and W. Weise. Resonances and higher
571 twist in polarized lepton nucleon scattering. *Nucl. Phys.*, A665:125–136, 2000. [8](#)
- 572 [6] K.G. Fissum et al. Vertical drift chambers for the hall a high-resolution
573 spectrometers at jefferson lab. *Nuclear Instruments and Methods in Physics*
574 *Research Section A: Accelerators, Spectrometers, Detectors and Associated*
575 *Equipment*, 474(2):108 – 131, 2001. [vi](#), [20](#), [22](#)
- 576 [7] David J. Flay. *Measurements of the Neutron Longitudinal Spin Asymmetry A1n*
577 *and Flavor Decomposition in the Valence Quark Region*. PhD thesis, Temple
578 University, Philadelphia, PA, Aug 2014. [vi](#), [2](#), [3](#), [16](#)

- 579 [8] D.F. Geesaman, K Saito, and A Thomas. The nuclear emc effect. *Annual Review*
580 *of Nuclear and Particle Science*, 45(1):337–390, 1995. [8](#)
- 581 [9] J. Gomez et al. Measurement of the A-dependence of deep inelastic electron
582 scattering. *Phys. Rev.*, D49:4348–4372, 1994. [8, 28](#)
- 583 [10] D. Higinbotham. The emc effect still puzzles after 30 years - cern courier.
584 <http://cerncourier.com/cws/article/cern/53091>, April 2013. (Visited on
585 01/04/2016). [vi, 2, 7, 9](#)
- 586 [11] Doug Higinbotham. Target images, December 2017. [18](#)
- 587 [12] R Hofstadter. Nuclear and nucleon scattering of high-energy electrons. *Annual*
588 *Review of Nuclear Science*, 7(1):231–316, 1957. [4](#)
- 589 [13] Henry W. Kendall. Deep inelastic scattering: Experiments on the proton and
590 the observation of scaling. *Rev. Mod. Phys.*, 63:597–614, Jul 1991. [6](#)
- 591 [14] Simona Malace, David Gaskell, Douglas W. Higinbotham, and Ian Cloet. The
592 Challenge of the EMC Effect: existing data and future directions. *Int. J. Mod.*
593 *Phys.*, E23:1430013, 2014. [6](#)
- 594 [15] R. W. McAllister and R. Hofstadter. Elastic scattering of 188-mev electrons from
595 the proton and the alpha particle. *Phys. Rev.*, 102:851–856, May 1956. [2](#)
- 596 [16] David Meekings. Hall a tritium target. , Thomas Jefferson Lab, Virginia,
597 engineering Report, 2017. [17](#)
- 598 [17] P R Norton. The emc effect. *Reports on Progress in Physics*, 66(8):1253, 2003.
599 [vi, 8](#)
- 600 [18] Bogdan Povh, Klaus Rith, Christoph Scholz, and Frank Zetsche. *Particles and*
601 *Nuclei: An Introduction to the Physical Concepts*. Springer, 2009. [1, 2, 4, 5](#)

- 602 [19] Tom Powers, Lawrence Doolittle, Rok Ursic, and Jeffrey Wagner. Design,
603 commissioning and operational results of wide dynamic range bpm switched
604 electrode electronics. *AIP Conference Proceedings*, 390(1):257–265, 1997. [13](#),
605 [24](#)
- 606 [20] J. Seely et al. New measurements of the european muon collaboration effect in
607 very light nuclei. *Phys. Rev. Lett.*, 103:202301, Nov 2009. [2](#), [8](#), [9](#)
- 608 [21] Richard E. Taylor. Deep inelastic scattering: The early years. *Rev. Mod. Phys.*,
609 63:573–595, Jul 1991. [6](#)
- 610 [22] Hall A Tech. Ep method. [http://hallaweb.jlab.org/equipment/beam/
611 energy/ep_web.html](http://hallaweb.jlab.org/equipment/beam/energy/ep_web.html). (Accessed on 06/28/2016). [16](#)
- 612 [23] Pengjia Zhu et al. Beam Position Reconstruction for the g2p Experiment in Hall
613 A at Jefferson Lab. *Nucl. Instrum. Meth.*, A808:1–10, 2016. [vi](#), [13](#), [14](#), [15](#), [24](#)

Appendix

614